Chemical Science

ROYAL SOCIETY OF CHEMISTRY

REVIEW

View Article Online
View Journal | View Issue

Cite this: *Chem. Sci.*, 2024, **15**, 20155

Photo-triggered NO release of nitrosyl complexes bearing first-row transition metals and therapeutic applications

Seungwon Sun, [a] Jisu Choe [a] and Jaeheung Cho *[ab]

In biological systems, nitric oxide (NO) is a crucial signaling molecule that regulates a wide range of physiological and pathological processes. Given the significance of NO, there has been considerable interest in delivering NO exogenously, particularly through light as a non-invasive therapeutic approach. However, due to the high reactivity and instability of NO under physiological conditions, directly delivering NO to targeted sites remains challenging. In recent decades, photo-responsive transition metal–nitrosyl complexes, especially based on first-row transition metals such as Mn, Fe, and Co, have emerged as efficient NO donors, offering higher delivery efficiency and quantum yields than heavy metal–nitrosyl complexes under light exposure. This review provides a comprehensive overview of current knowledge and recent developments in the field of photolabile first-row transition metal–nitrosyl complexes, focusing on the structural and electronic properties, photoreactivity, photodissociation mechanisms, and potential therapeutic applications. By consolidating the key features of photoactive nitrosyl complexes, the review offers deeper insights and highlights the potential of first-row transition metal–nitrosyl complexes as versatile tools for photo-triggered NO delivery.

Received 8th October 2024
Accepted 6th November 2024

DOI: 10.1039/d4sc06820c

rsc.li/chemical-science

1. Introduction

Nitric oxide (NO), an endogenously generated gaseous signaling molecule, plays an important role in various physiological and pathophysiological processes in biological systems. Over the past few decades, NO has attracted significant attention due to diverse biological roles. The importance of NO was highlighted in 1998 when Louis J. Ignarro, Robert F. Furchgott, and F. Murad were awarded the Nobel Prize for the discovery of NO as an endothelial-derived relaxation factor (EDRF), which regulates vasodilation in smooth muscle cells and contributes to lower blood pressure.[1,2] After the discovery of the vasorelaxation effect by NO, subsequent research has expanded our understanding of the physiological functions of NO, revealing involvement in neurotransmission, immune defense, and other critical biological processes.[3–5]

NO is tightly and precisely regulated in biological systems, where NO performs a variety of essential functions depending

[a]*Department of Chemistry, Ulsan National Institute of Science and Technology (UNIST), Ulsan 44919, Republic of Korea. E-mail: jaeheung@unist.ac.kr*
[b]*Graduate School of Carbon Neutrality, Ulsan National Institute of Science and Technology (UNIST), Ulsan 44919, Republic of Korea*

Seungwon Sun

Seungwon Sun completed his BS degree in Chemistry at Chungnam National University in 2020. He is currently an integrated MS–PhD candidate under the supervision of Professor Jaeheung Cho at the Ulsan National Institute of Science and Technology (UNIST). His research focuses on nitric oxide delivery and mechanistic investigations of metalloenzymes through biomimetic systems.

Jisu Choe

Jisu Choe received his PhD degree from Daegu Gyeongbuk Institute of Science and Technology (DGIST) in 2023. He is currently a postdoctoral researcher in the Department of Chemistry at Ulsan National Institute of Science and Technology (UNIST). His research focuses on the design and synthesis of metal–nitrosyl complexes with first-row transition metals and optimization of photolabile NO donors for applications in biological systems.

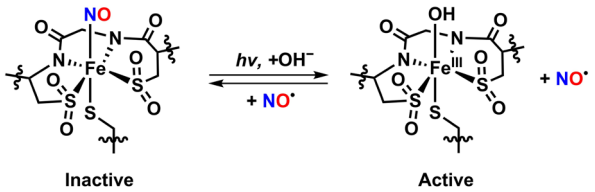

Scheme 1 Photo-regulated transformation between the active and inactive forms of the Fe-NHase enzyme for catalytic reaction. NO reversibly interacts with the nonheme Fe center.

on its concentration. At nanomolar (nM) levels, NO modulates neurotransmission and blood pressure, while at micromolar (μM) concentrations, NO acts as an immune defense agent against invading pathogens.[6,7] The multifaceted roles of NO are primarily mediated by chemical interactions with transition metal sites in metalloenzymes. In the vasodilation process, for example, NO interacts with an iron site in soluble guanylate cyclase (sGC). NO diffuses across the cell membrane and coordinates to the heme site in sGC, leading to the generation of cyclic guanosine-3′,5′-monophosphate (cGMP), which facilitates blood pressure relaxation.[8,9]

Beyond the roles of NO in mammals, NO regulates enzymatic processes in bacteria. A prominent example is an iron-containing nitrile hydratase (Fe-NHase), a metalloenzyme found in microorganisms such as *Rhodococcus* sp. N-771, N-774, and R-312. Fe-NHase catalyzes the conversion of organic nitriles into amides *via* hydrolysis reaction, which is photo-regulated by the reversible interaction of NO with the nonheme Fe center as shown in Scheme 1. In the absence of light, NO binds to the Fe active site to form a nitrosylated complex in a catalytically inactive form. Upon exposure to light, the Fe–NO bond is cleaved, restoring catalytic activity by generating a reactive Fe^{III}–hydroxo (Fe^{III}–OH) intermediate.[10–12]

The diverse biological roles of NO and photoactivation of Fe–NO bond have spurred significant interest in developing NO delivery systems for therapeutic applications.[13] However, artificially controlling NO concentration in biological systems remains challenging due to the very short half-life time and high reactivity of NO under physiological conditions. To overcome the aforementioned limitation of NO delivery, various NO donors have been explored, including organic nitrates (RO-NO_2), *S*-nitrosothiols (RSNOs), *N*-diazeniumdiolates (NONOates), and transition metal-based NO donors.[14–21] While organic NO donors have been approved for clinical uses, spontaneous NO release in biological environments complicates the precise control of NO concentrations at target sites. In contrast, transition metal–nitrosyl (M–NO) complexes have attracted attention for the ability to offer thermodynamic stability to NO by coordinating with metal centers, allowing for selective delivery through external stimuli such as light, solvation, pH, and heat.[22,23] Among the numerous transition metals, first-row transition ions are preferred for medical applications because of the relatively lower cytotoxicity compared to heavy metals such as ruthenium (Ru),[24–26] platinum (Pt),[27,28] palladium (Pd),[29] and osmium (Os).[30,31] Moreover, first-row transition M–NO complexes bearing manganese (Mn), iron (Fe), and cobalt (Co) represent a particularly promising approach, offering a non-invasiveness and easily controllable method for precise spatiotemporal control of NO delivery.

Identification and characterization of nitrosyl complexes are essential in bioinorganic chemistry to enhance our understanding of the chemical properties of M–NO complexes and photodissociation reactions. Although several review articles have examined photoactive M–NO complexes, the majority have focused primarily on ruthenium–nitrosyl (Ru–NO) complexes, with comparatively less attention given to manganese–nitrosyl (Mn–NO) and iron–nitrosyl (Fe–NO) complexes.[22,26,32–35] This review aims to provide a comprehensive overview of the latest research trends on photoactive nitrosyl complexes containing first-low transition metals such as Mn, Fe, and Co. The review will cover essential geometric and electronic structures, photoreactivity, and computational studies on photodissociation mechanisms. Additionally, the factors influencing photolability will be discussed. By taking comprehensive approach to M–NO adducts, the review seeks to offer a deeper understanding of the nature and properties of light-sensitive M–NO species.

Jaeheung Cho

Jaeheung Cho received his PhD degree in inorganic chemistry from Kanazawa University in Japan (2005), under the supervision of Prof. Masatatsu Suzuki. He then completed a postdoctoral fellowship at the University of Delaware in US (2005–2007). Upon returning to Korea, he joined Ewha Womans University as a Full-Time Lecturer and Specially Appointed Professor (2007–2012). In 2012, he began his independent career at DGIST, where he served as an Assistant Professor and later became an Associate Professor in 2017. He joined the Department of Chemistry at UNIST as a Professor in 2020. His research focuses on synthetic bioinorganic chemistry for catalysis and drug discovery.

2. Synthesis, characterization, and photoreactivity of M–NO complexes

2.1 Generation of M–NO complexes

Inspired by the regulatory roles of NO in biological systems and the photolability observed in Fe-NHase enzymes, a variety of photoactive mononitrosyl complexes containing first-row transition metals such as Mn,[36–40] Fe,[41–54] and Co[55] have been synthesized and characterized to understand physical and chemical properties, as well as photoreactivity. All supporting ligands used for the synthesis of photoactive M–NO complexes, as discussed in this review, are illustrated in Chart 1.

A common method for synthesizing M–NO species involves introducing purified NO gas into a solution of precursor

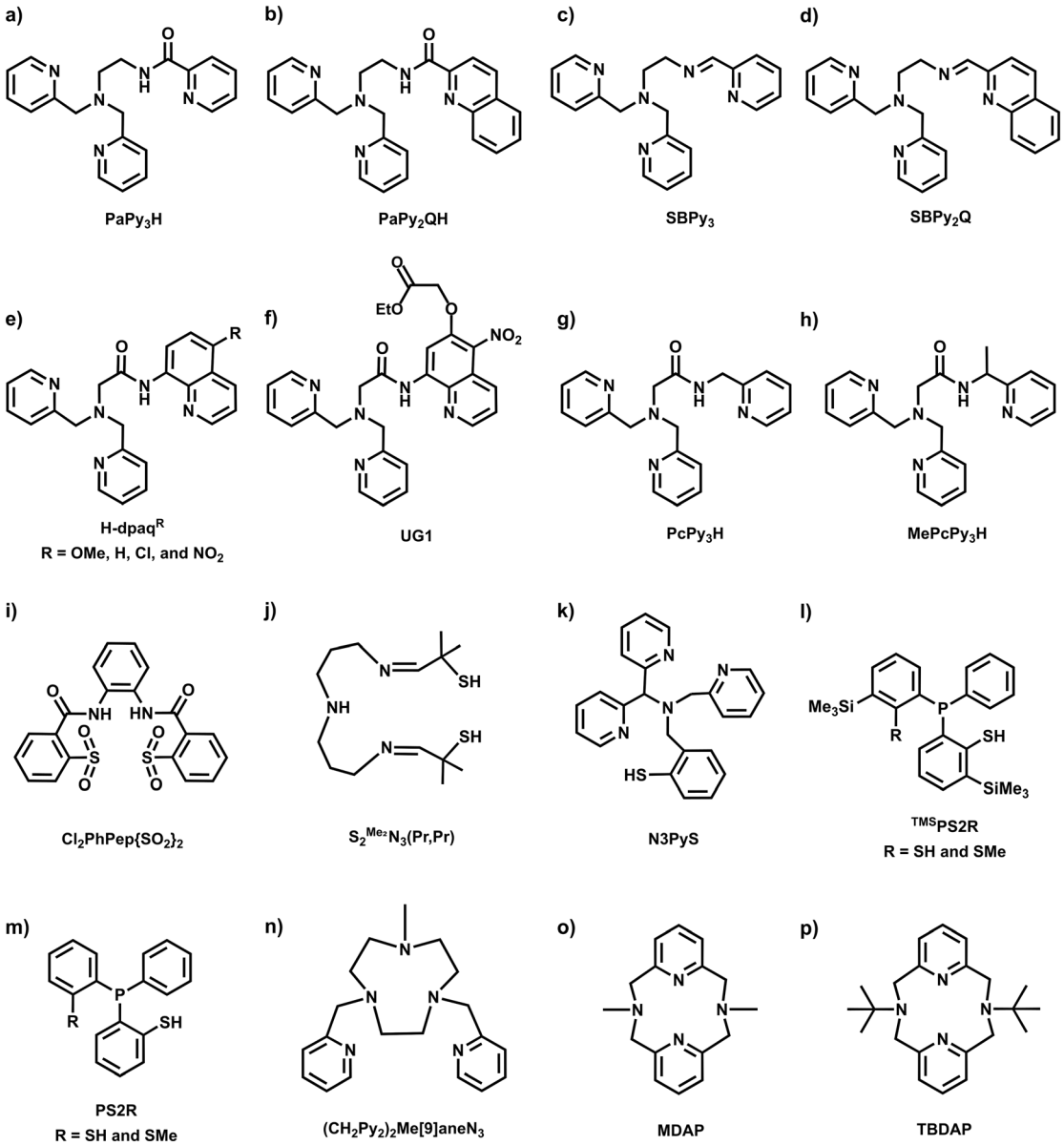

Chart 1 Ligand structures discussed in this review.

complexes under inert conditions.[36–49] Alternative strategies include employing redox reactions of existing nitrosyl complexes[50] or utilizing commercially available nitrosylated metal sources.[52,53] Transition metal ions in the 2+ or 3+ oxidation states are typically used to generate $\{MNO\}^n$ complexes, based on Enemark–Feltham notation, where n represents the total number of electrons in the metal d orbitals and NO π^* orbitals (Scheme 2).[56] After nitrosyl complexes are generated in solution, the resulting species are crystallized and characterized using various physicochemical methods such as ultraviolet-visible (UV-vis) spectroscopy, infrared (IR) spectroscopy, proton nuclear magnetic resonance (^{1}H NMR) spectroscopy, electron paramagnetic resonance (EPR) spectroscopy, Mössbauer spectroscopy, and single crystal X-ray diffractometry (SC-XRD).

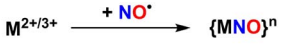

M = Mn, Fe, and Co
n = # of electrons in metal d orbitals + NO π^* orbitals

Scheme 2 Synthetic strategies for the generation of M–NO complexes.

2.2 Manganese–nitrosyl complexes

Photoactive manganese–nitrosyl (Mn–NO) species have been suggested as potent NO-releasing agents. The Mn–NO complexes are synthesized from Mn(II) precursors, resulting in the formation of low-spin $S = 0$ $\{MnNO\}^6$ species.[36–40] The thermal stability of Mn–NO adducts in the absence of light has allowed researchers to scrutinize electronic and structural properties. Additionally, photoreactivity studies in various solvents have demonstrated that Mn–NO complexes can selectively release NO at targeted sites through the photodissociation

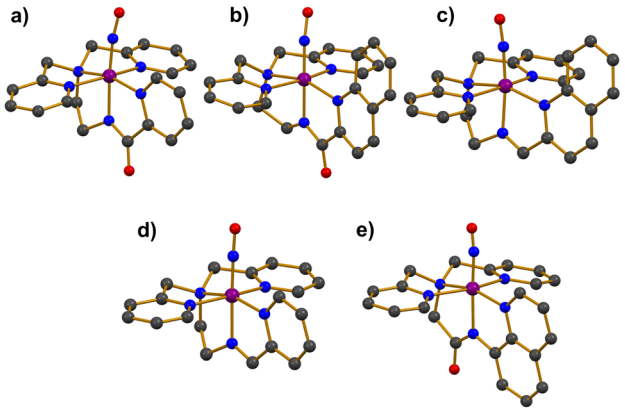

Fig. 1 Crystal structures of Mn–NO complexes: (a) $[Mn(PaPy_3)(NO)]^+$ (**1**), (b) $[Mn(PaPy_2Q)(NO)]^+$ (**2**), (c) $[Mn(SBPy_3)(NO)]^{2+}$ (**3**), (d) $[Mn(SBPy_2Q)(NO)]^{2+}$ (**4**), and (e) $[Mn(dpaq^H)(NO)]^+$ ($\mathbf{5^H}$) (dark grey, C; blue, N; red, O; purple, Mn).

of the Mn–NO bond, presenting significant potential for biomedical applications.

The first photolabile complex, $[Mn(PaPy_3)(NO)]^+$ (**1**), bearing a deprotonated anionic pentadentate N5 carboxamide ligand (Chart 1a) was reported.[36] The introduction of purified NO gas to a CH_3CN solution of $[Mn^{II}(PaPy_3)(H_2O)]^+$ led to the formation of complex **1**, which exhibited UV-vis absorption bands at 420, 440, and 635 nm. The spin state of **1** was determined to be in the $S = 0$ ground state by ^1H NMR spectroscopy, with displayed diamagnetic resonance peaks within the range of 0–10 ppm. Single crystal X-ray structure exhibited a mononuclear and six-coordinate distorted octahedral geometry with the NO ligand positioned *trans* to the anionic carboxamide nitrogen donor of the supporting ligand (Fig. 1a). The Mn–NO and N–O bond lengths were measured at 1.6601 and 1.1928 Å, respectively, with a Mn–N–O bond angle of 171.91°. The IR spectrum of **1** showed a strong NO stretching vibration band at 1745 cm^{-1}, which is consistent with typical diamagnetic $\{MnNO\}^6$ complexes (1700–1775 cm^{-1}).

The photolysis of **1** was investigated across a broad range of wavelengths (380–810 nm) and light intensities.[36,38] The highest quantum yield was achieved with 500 nm light irradiation, resulting in the formation of a solvated Mn(III) species, which is the oxidized form of the corresponding NO-released Mn(II) complex under aerobic conditions. The reaction kinetics followed pseudo-first-order behavior in various solvents such as CH_3CN, DMF, and H_2O, showing different rate constants (CH_3CN > DMF > H_2O). Additionally, the NO dissociation rate increased proportionally with light intensity.

Another photoactive complex, $[Mn(PaPy_2Q)(NO)]^+$ (**2**), was synthesized by reacting excess NO gas with the Mn(II) starting complex of $[Mn^{II}(PaPy_2Q)(H_2O)]^+$ in CH_3CN.[37] The UV-vis absorption band of **2** was red-shifted to 650 nm compared to 635 nm for **1**. In addition, the extinction coefficient of **2** was nearly double that of **1** (Table 1). The red-shift and enhanced light absorption were attributed to the modification of the ligand system, where the pyridine group in **1** was replaced by a quinoline group, a more conjugated ring system (Chart 1a *versus* 1b). Consequently, the increased π-conjugation on the supporting ligand enhanced the light responsiveness of **2** (*vide infra*). The $S = 0$ ground state of **2** was confirmed by ^1H NMR spectroscopy, indicating that **2** is a diamagnetic species. The X-ray diffraction analysis of **2** revealed similar coordination geometry with **1** as shown in Fig. 1b.[36] The slightly longer Mn–NO and N–O bond distances of 1.678 and 1.237 Å, respectively, were accompanied with a linear Mn–N–O angle of 171.5°. The elongation of the bond length in **2** resulted in a lower NO vibration energy, observed at 1725 cm^{-1}.

The photo-triggered NO release from **2** was observed in both CH_3CN and H_2O under visible light irradiation.[37,38] The UV-vis spectral change of **2** indicated that NO was dissociated from the Mn center, regenerating the Mn(II) precursor species. The photochemical kinetics obeyed pseudo-first-order behavior in all solvents, showing almost two times higher quantum yield of **1** under the same wavelength of light (Table 3).

Two additional complexes, $[Mn(SBPy_3)(NO)]^{2+}$ (**3**) and $[Mn(SBPy_2Q)(NO)]^{2+}$ (**4**), supported by neutral pentadentate N5 Schiff base ligands (Chart 1c and d), were synthesized by reacting

Table 1 Selected spectroscopic and geometric data of Mn–NO complexes

	UV-vis		Bond lengths	Bond angle	
Mn–NO complex	λ [nm] (ε [M^{-1} cm^{-1}])	IR [cm^{-1}]	Mn–NO/N–O [Å]	M–N–O [°]	Ref.
$[Mn(PaPy_3)(NO)]^+$ (**1**)	420(3320), 440(3300), 635(220)[a]	1745[d]	1.6601/1.1918	171.91	36
$[Mn(PaPy_2Q)(NO)]^+$ (**2**)	240(29 500), 290(7700), 495(2030), 650(420)[a]	1725[d]	1.678/1.237	171.5	37
$[Mn(SBPy_3)(NO)]^{2+}$ (**3**)	340(1725), 500(1990), 720(750)[a]	1773[d]	1.649/1.167	177.2	38
$[Mn(SBPy_2Q)(NO)]^{2+}$ (**4**)	330(12 850), 550(2100), 785(1200)[a]	1759[d]	1.651/1.179	175.3	38
$[Mn(dpaq^{OMe})(NO)]^+$ ($\mathbf{5^{OMe}}$)	398(3830), 457(4230)[b]	1737[e]	1.742/1.015	176.7	39
$[Mn(dpaq^{H})(NO)]^+$ ($\mathbf{5^{H}}$)	357(3910), 461(3120)[b]	1739[e]	1.635/1.022	171	39
$[Mn(dpaq^{Cl})(NO)]^+$ ($\mathbf{5^{Cl}}$)	375(4560), 475(2960)[b]	1743[e]	1.713/1.044	171.3	39
$[Mn(dpaq^{NO_2})(NO)]^+$ ($\mathbf{5^{NO_2}}$)	392(10 300), 523(1570)[b]	1744[e]	1.660/1.136	175.8	39
UG1NO (**6**)	385(8300), 494(2700)[c]	1746[e]	—	—	40

[a] UV-vis absorption bands in CH_3CN. [b] UV-vis absorption bands in MES buffer = 2-(*N*-morpholino)ethanesulfonic acid (pH 7.2, 5% DMSO). [c] UV-vis absorption bands in H_2O. [d] IR spectrum with KBr pellet. [e] IR spectrum with ATR-IR.

Table 2 Selected spectroscopic and geometric data of Fe–NO complexes

Fe–NO complex	Enemark–Feltham notation	UV-vis λ [nm] (ε [M^{-1} cm^{-1}])	IR [cm^{-1}]	Spin state	Bond lengths Fe–NO/N–O [Å]	Bond angle M–N–O [°]	Ref.
$[FeS_2{}^{Me_2}N_3(Pr,Pr)(NO)]^+$ (**7**)	{FeNO}^{6}	420(1700)[a]	1822[e]	$S = 0$	1.676/1.161	172.3	41
$[Fe(PaPy_3)(NO)]^{2+}$ (**8**)	{FeNO}^{6}	365(1850), 500(1050)[a]	1919[e]	$S = 0$	1.677/1.139	173.1	42 and 43
$[Fe(PcPy_3)(NO)]^{2+}$ (**9**)	{FeNO}^{6}	363(2040), 500(925)[a]	1897[e]	$S = 0$	1.680/1.147	177.3	44
$[Fe(MePcPy_3)(NO)]^{2+}$ (**10**)	{FeNO}^{6}	360(2012), 505(735)[a]	1918[e]	$S = 0$	1.678/1.147	177.6	44
$[Fe(PaPy_2Q)(NO)]^{2+}$ (**11**)	{FeNO}^{6}	310(83 400), 330(83 000), 510(10 100)[a]	1885[e]	$S = 0$	1.6817/ 1.1435	166.66	45
$[Fe(Cl_2PhPep\{SO_2\}_2)(NO)(DMAP)]^-$ (**12**)	{FeNO}^{6}	440[a]	1854[e]	$S = 0$	—	—	46 and 47
$[Fe(N3PyS)(NO)]^+$ (**13**)	{FeNO}^{7}	350(5300), 440(2400), 540(970)[a]	1660[f] 1753[f]	$S = 1/2$[i] $S = 3/2$[j]	1.7327/1.15[i] 1.747/1.14[j]	147.2[i] 161.11[j]	48 and 49
$[Fe(N3PyS)(NO)]^{2+}$ (**14**)	{FeNO}^{6}	342(12 200), 636(820)[a]	1909[g]	$S = 0$	1.69[h]	—	50
$[Fe((CH_2Py_2)_2Me[9]aneN_3)(NO)]^{2+}$ (**15**)	{FeNO}^{7}	242(21 000), 318(36 000)[a]	1660[f]	$S = 1/2$	1.731/1.143	148.3	51
$[Fe(^{TMS}PS2)(^{TMS}PS2H)(NO)]$ (**16**)	{FeNO}^{6}	480(1810), 630(755)[b]	1829[e]	$S = 0$	1.644/1.153	177.3	52
$[Fe(^{TMS}PS2)(^{TMS}PS2CH_3)(NO)]$ (**17**)	{FeNO}^{6}	480(1760), 630(705)[b]	1822[e]	$S = 0$	1.642/1.152	176.1	52
[Fe(PS2)(PS2H)(NO)] (**18**)	{FeNO}^{6}	480(1810), 630(755)[c]	1832[e]	$S = 0$	1.6513/1.152	175.56	53
$[Fe(PS2)(PS2CH_3)(NO)]$ (**19**)	{FeNO}^{6}	480(1760), 630(705)[c]	1832[e]	$S = 0$	1.6449/1.150	175.05	53
$[Fe(TBDAP)(NO)(H_2O)]^{2+}$ (**20**)	{FeNO}^{7}	407(1100), 522(320), 745(97)[d]	1781[f]	$S = 3/2$	1.754/1.153	152.9	54

[a] UV-vis absorption bands in CH_3CN. [b] UV-vis absorption bands in toluene. [c] UV-vis absorption bands in CH_2Cl_2. [d] UV-vis absorption bands in acetone. [e] IR spectrum with KBr pellet. [f] IR spectrum with ATR-IR. [g] Low temperature FTIR at 15 K in CH_2Cl_2. [h] Obtained from EXAFS. [i] Measured at 110 K. [j] Measured at 293 K.

NO gas with the Mn(II) precursor complexes, $[Mn^{II}(SBPy_3)(MeOH)]^{2+}$ and $[Mn^{II}(SBPy_2Q)(EtOH)]^{2+}$.[38] The coordination environments around Mn center in **3** and **4** were characterized by X-ray diffraction analysis (Fig. 1c and d). In both complexes, the NO ligand was coordinated *trans* to the imine nitrogen donor of the supporting ligands, displaying linear Mn–N–O bond angles (Table 1). The N–O bond lengths were measured as 1.167 Å for **3** and 1.179 Å for **4**, while the Mn–NO bond lengths were determined to be 1.649 and 1.651 Å, respectively. The shorter N–O bond in **3** corresponds to a higher NO stretching frequency of 1773 cm^{-1}, compared to 1759 cm^{-1} for **4**. The UV-vis absorption bands of **4** were red-shifted relative to those of **3** (500 and 720 nm for **3**; 550 and 780 nm for **4**), along with enhanced absorptivity (Table 1). The shifts in absorption bands and increased absorbance were attributed to the presence of the additional conjugated quinoline ring in the ligand system (Chart 1c *versus* 1d), similar to the behavior observed in complexes **1** and **2**.

Near-infrared (NIR) light responsiveness was observed in the photolysis of **3** and **4**, which released NO under NIR light (800–950 nm) in CH_3CN and aqueous solutions, differing from the photolysis of **1** and **2**.[36–38] The NIR responsiveness was attributed to the coordination of the imine ligand, which modulates the absorption bands to shift to longer wavelengths and increases the extinction coefficient (*vide infra*). Sensitivity to NIR light is noteworthy because NIR light can effectively penetrate human skin without causing damage.

The electronic effects on NO release, influenced by substituting functional groups in ligand frameworks, were systematically investigated.[39] To explore the electronic effects, a series of four Mn–NO complexes, $[Mn(dpaq^R)(NO)]^+$ ($\mathbf{5}^R$, R = OMe, H, Cl, and NO_2), containing anionic pentadentate N5 carboxamide ligands (Chart 1e) were synthesized by bubbling purified NO gas into CH_3CN solutions of the precursor complexes. SC-XRD analysis revealed that all nitrosyl complexes exhibited distorted octahedral geometries. The geometric parameters and vibration energies of N–O bond are listed in Table 1. All complexes released NO under light irradiation, displaying varying dissociation rates. The impact of the substituents on the photodissociation reaction and electronic structure will be discussed (*vide infra*).

Later, an additional electron-donating ethyl ester group was introduced at the 6-position of the quinoline ring in the $dpaq^{NO_2}$ ligand of complex $\mathbf{5}^{NO_2}$ (Chart 1f) to produce the UG1NO (**6**).[40] Upon adding purified NO gas to the Mn(II) starting complex, $[Mn^{II}(UG1)]^+$, in a CH_3CN/MeOH mixture, dark red species of **6** were precipitated. Although single crystals could not be obtained, ESI-MS analysis supported the generation of **6** with an ion peak at a mass-to-charge ratio (m/z) of 614.31, corresponding to **6**. The UV-vis spectrum of **6** exhibited absorption bands at 385 and 494 nm in aqueous solution, while the IR spectrum showed a NO stretching vibration at 1746 cm^{-1}.

Complex **6** remained stable in a buffer solution at pH 7.2 when kept in the dark. However, upon exposure to 650 nm light, **6** rapidly decomposed back to the corresponding Mn(II) starting complex due to NO loss from the Mn center with a quantum yield of 0.74 (Table 3). Complex **6** exhibited light absorption in the visible-NIR region and displayed a similar response to light irradiation as $\mathbf{5}^{NO_2}$, despite the presence of the additional electron-donating ethyl ester moiety on the quinoline ring.

Table 3 Quantum yields (ϕ_{NO}) of M–NO complexes

Nitrosyl complex	Solvent	λ_{irr} [nm]	ϕ_{NO} [mol per einst]	Ref.
$[Mn(PaPy_3)(NO)]^+$ (**1**)	CH_3CN	500	0.326	36 and 38
		550	0.309	
	H_2O	500	0.400	
		550	0.385	
$[Mn(PaPy_2Q)(NO)]^+$ (**2**)	CH_3CN	500	0.623	37 and 38
		550	0.579	
	H_2O	500	0.742	
		550	0.694	
$[Mn(SBPy_3)(NO)]^{2+}$ (**3**)	CH_3CN	500	0.411	38
		550	0.580	
$[Mn(SBPy_2Q)(NO)]^{2+}$ (**4**)	CH_3CN	500	0.393	38
		550	0.434	
$[Mn(dpaq^{OMe})(NO)]^+$ ($\mathbf{5}^{OMe}$)	MES buffer[a]	460	0.58	39
		530	0.47	
		650	0.49	
$[Mn(dpaq^{H})(NO)]^+$ ($\mathbf{5}^{H}$)	MES buffer[a]	460	0.61	39
		530	0.51	
		650	0.47	
$[Mn(dpaq^{Cl})(NO)]^+$ ($\mathbf{5}^{Cl}$)	MES buffer[a]	460	0.66	39
		530	0.66	
		650	0.73	
$[Mn(dpaq^{NO_2})(NO)]^+$ ($\mathbf{5}^{NO_2}$)	MES buffer[a]	460	0.61	39
		530	0.63	
		650	0.78	
UG1NO (**6**)	MES buffer[a]	650	0.74	40
$[Fe(PaPy_3)(NO)]^{2+}$ (**8**)	CH_3CN	500	0.185	42 and 43
$[Fe(PaPy_2Q)(NO)]^{2+}$ (**11**)	CH_3CN	500	0.258	45
$[Fe(Cl_2PhPep\{SO_2\}_2)(NO)(DMAP)]^-$ (**12**)	CH_3CN	450	0.55	46 and 47
$[Fe(TBDAP)(NO)(H_2O)]^{2+}$ (**20**)	H_2O	White light	0.23	54
$[Co(MDAP)(NO)(CH_3CN)]^{2+}$ (**21**)	H_2O	White light	0.78	55

[a] MES = 2-(*N*-morpholino)ethanesulfonic acid (pH 7.2, 5% DMSO).

2.3 Iron–nitrosyl complexes

Photolabile iron–nitrosyl (Fe–NO) complexes have garnered significant attention as promising NO transfer agents for biomedical treatments and as biomimetic models of the Fe-NHase enzymes. Accordingly, extensive research has focused on the synthetic Fe–NO complexes. As illustrated in Scheme 2, Fe–NO adducts are commonly synthesized by reacting NO gas with Fe precursors in the Fe(II) or Fe(III) oxidation states, followed by characterization using various physicochemical methods.[41–54]

The photolabile complex, $[FeS_2{}^{Me_2}N_3(Pr,Pr)(NO)]^+$ (**7**), bearing a pentadentate thiolate ligand (Chart 1j) was reported.[41] Treating a solution of the precursor complex, $[Fe^{III}S_2{}^{Me_2}N_3(Pr,Pr)]^+$, with excess NO gas afforded **7**. Upon the addition of NO to the starting complex, a UV-vis absorption band appeared at 420 nm in CH_3CN at room temperature and the redox potential decreased from −400 to −455 mV (*vs.* SCE), implying that the Fe(III) center was stabilized by NO coordination. X-ray crystallography revealed a distorted octahedral geometry for **7**, with the NO ligand coordinated *trans* to the thiolate donor (Fig. 2a). The Fe–N–O bond angle was found to be linear at 172.3°, while the Fe–NO and N–O bond distances were measured as 1.676 and 1.161 Å, respectively. The NO stretching vibration band in the IR spectrum was observed at 1822 cm^{-1}, which is close to that of the inactive NO-bound Fe-NHase enzyme (ν_{NO} = 1853 cm^{-1}). The diamagnetic ^1H NMR signal of **7** indicated antiferromagnetic coupling between the low-spin $S = 1/2$ Fe(III) and the $S = 1/2$ NO radical.

Photodissociation of **7** was demonstrated by illuminating a CH_3CN solution of the complex under inert conditions with

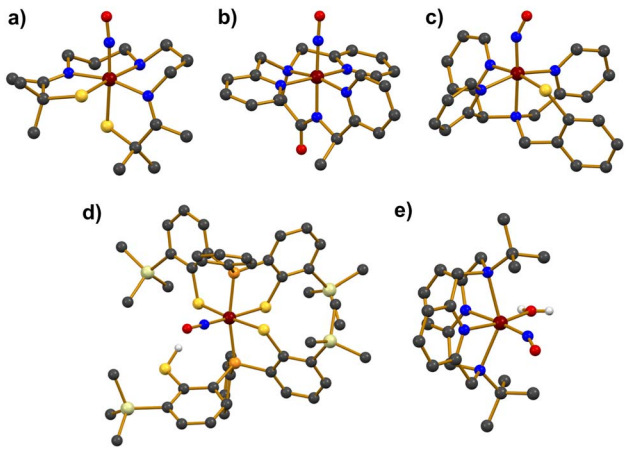

Fig. 2 Crystal structures of Fe–NO complexes, (a) $[FeS_2{}^{Me_2}N_3(Pr,Pr)(NO)]^+$ (**7**), (b) $[Fe(MePcPy_3)(NO)]^{2+}$ (**10**), (c) $[Fe(N3PyS)(NO)]^+$ (**13**), (d) $[Fe(^{TMS}PS2)(^{TMS}PS2H)(NO)]$ (**16**), and (e) $[Fe(TBDAP)(NO)(H_2O)]^{2+}$ (**20**) (dark grey, C; blue, N; red, O; yellow, S; scarlet, Fe).

a Hg lamp, applied at slightly reduced pressure. Light exposure cleaved the Fe–NO bond, releasing a free NO radical and regenerating the starting Fe(III) complex. The release of NO gas was further confirmed by mass spectrometric analysis of the headspace gases.

A photoactive nitrosyl complex, $[Fe(PaPy_3)(NO)]^{2+}$ (**8**), a Fe analogue of **1**, was synthesized. Addition of NO to a solution of $[Fe^{III}(PaPy_3)(CH_3CN)]^{2+}$ resulted in the formation of the $\{FeNO\}^6$ complex.[42,43] The coordination environment was found to be comparable to that of **1**, featuring a distorted octahedral geometry with a linear Fe–N–O bond angle of 173.1°. The NO ligand occupied one coordination site with Fe–NO and N–O bond lengths of 1.677 and 1.139 Å, respectively. The IR spectrum displayed a NO stretching band at 1919 cm^{-1}, which falls within the typical range for $\{FeNO\}^6$ complexes (1850–1940 cm^{-1}). The diamagnetic signal in the ^1H NMR spectrum in CD_3CN, along with isomer shift (δ) of −0.05 mm s^{-1} and quadrupole splitting (ΔE_Q) of +0.85 mm s^{-1} in the zero-field Mössbauer spectrum at 4.2 K, indicated an Fe^{II}–NO^+ electronic configuration for **8**.

Photolysis of **8** under visible light (tungsten lamp, 50 W) caused a rapid color change with isosbestic points observed at 484, 392, and 334 nm in the UV-vis spectrum.[43] The final UV-vis absorption band suggested the formation of an Fe(III) precursor species, indicating NO release. The photolysis kinetics in various solvents such as CH_3CN, H_2O, and DMF followed pseudo-first-order behavior with the rate of NO dissociation increasing proportionally to the light intensity.

Two additional complexes, $[Fe(PcPy_3)(NO)]^{2+}$ (**9**) and $[Fe(MePcPy_3)(NO)]^{2+}$ (**10**), were prepared by reacting NO gas with the Fe(III) precursor complexes, which are supported by the anionic pentadentate N5 carboxamide ligands $PcPy_3H$ (Chart 1g) and $MePcPy_3H$ (Chart 1h).[44] The binding of NO to the Fe center produced diamagnetic signals of ^1H NMR, indicating $S = 0$ ground states for both complexes. The coordination environments around the Fe center in both complexes showed similar features to that observed in **8**, with NO binding to Fe in a linear Fe–N–O arrangement (177.3° for **9** and 177.6° for **10**) (Fig. 2b). The Fe–NO and N–O bond lengths of **9** were measured as 1.680 and 1.147 Å, respectively. For **10**, almost identical bond distances of Fe–NO and N–O were determined to be 1.678 and 1.147 Å, respectively. The NO stretching frequencies were 1897 cm^{-1} for **9** and 1918 cm^{-1} for **10**, which are typical for $\{FeNO\}^6$ complexes.

Under light illumination, complexes **9** and **10** demonstrated slightly faster NO release rates compared to **8** in CH_3CN. The NO dissociation followed pseudo-first-order kinetics, leading to the formation of solvated Fe(III) species. The NO dissociation rates were also dependent on light intensity, showing a linear increase with higher light power.

To verify the conjugation effect seen in Mn–NO complexes **1**–**4**, a modified complex, $[Fe(PaPy_2Q)(NO)]^{2+}$ (**11**), was synthesized by replacing the pyridine group in **8** with a quinoline ring (Chart 1b).[45] Reacting NO gas with the Fe(III) precursor complex, $[Fe(PaPy_2Q)(EtOH)]^{2+}$, yielded a dark purple product of **11**. The X-ray crystal structure showed a similarity to that of **8**. The IR spectrum of **11** exhibited an NO stretching vibration energy at 1885 cm^{-1}, close to the vibration energy of the free NO radical (1875 cm^{-1}). The N–O bond distance in **11** (1.1435 Å) was also similar to that of the free NO radical (1.15 Å), suggesting minimal back-donation from the Fe center to the bound NO.

The photolability of NO in **11** was examined in CH_3CN solution. Upon exposure to visible light (500 nm, 5 mW), the CH_3CN solution of **11** decomposed back to the starting complex, $[Fe^{III}(PaPy_2Q)(CH_3CN)]^{2+}$, as evidenced by the disappearance of the UV-vis absorption band at 510 nm with the isosbestic points at 375 and 690 nm. To evaluate the impact of replacing the pyridine group in **8** with a quinoline group in **11**, the quantum yields were compared. Complex **11** exhibited a higher quantum yield ($\phi_{NO} = 0.258$) than **8** ($\phi_{NO} = 0.185$), demonstrating that the increased conjugation from the quinoline group enhances light absorptivity and improves the quantum yield of the nitrosyl complex (Table 3).

An Fe–NO complex, $[Fe(Cl_2PhPepS)(NO)(DMAP)]^-$, was synthesized using a tetradentate N2S2 ligand.[46,47] The complex was obtained by reacting the starting complex of $[Fe(Cl_2PhPepS)(DMAP)]^-$ with NO gas in CH_3CN at −40 °C. The crystal structure of $[Fe(Cl_2PhPepS)(NO)(DMAP)]^-$ revealed an extremely distorted geometry with DMAP (*N*,*N*-dimethylaminopyridine) and NO ligand positioned axially. The Fe–NO and N–O bond distances were determined to be 1.612 and 1.167 Å, respectively, with a nearly linear Fe–N–O bond angle of 173.2°. The IR spectrum of $[Fe(Cl_2PhPepS)(NO)(DMAP)]^-$ showed a strong ν_{NO} stretch at 1849 cm^{-1}. While light-triggered NO release was not observed for $[Fe(Cl_2PhPepS)(NO)(DMAP)]^-$, NO dissociation occurred in coordinating solvents such as CH_3CN, THF, and DMF due to ligand

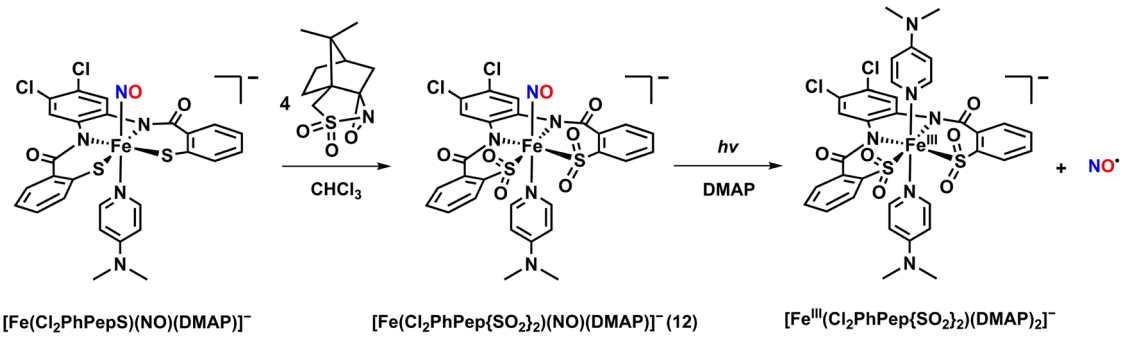

Scheme 3 *S*-Oxygenation reaction to yield the photoactive $\{FeNO\}^6$ complex **12** and photodissociation.

exchange reactions, where the NO ligand was replaced by solvent molecules. In contrast, $[Fe(Cl_2PhPepS)(NO)(DMAP)]^-$ remained stable in non-coordinating solvents like $CHCl_3$ or CH_2Cl_2.

To mimic the ligand backbone of the Fe-NHase enzyme, the thiolate (–S) groups in $[Fe(Cl_2PhPepS)(NO)(DMAP)]^-$ were oxygenated to form sulfinates ($-SO_2$) by treating the complex with 4 equivalents of (1*S*)-(+)-(10-camphorsulfonyl)oxaziridine in $CHCl_3$ at −40 °C in the absence of light. The reaction produced a pale-orange species, $[Fe(Cl_2PhPep\{SO_2\}_2)(NO)(DMAP)]^-$ (**12**), featuring a *S*-oxygenated supporting ligand (Chart 1i and Scheme 3). Complex **12** exhibited a UV-vis absorption band at 440 nm, which is very similar to the absorption band of the NO-bound Fe-NHase enzyme (400 nm). The instability of **12** prevented crystallization for X-ray diffraction analysis. However, the IR spectrum of **12** showed a ν_{NO} value of 1854 cm^{-1}, which is close to that of the inactivated Fe-NHase (1853 cm^{-1}), along with *S*-oxygenated bands at 1078, 1046, and 1007 cm^{-1}.

Interestingly, when a CH_3CN or $CHCl_3$ solution of **12** was exposed to visible light (10 mW) at −40 °C, the UV-vis spectrum showed immediate change, appearing a new band at 650 nm, indicating the release of NO. The quantum yield ($\lambda_{irr} = 450$ nm) for NO release was determined to be 0.55 (Table 3), which is comparable to that of Fe-NHase ($\phi_{NO} = 0.48$). The released free NO was detected using a NO-sensitive electrode. The X-band EPR spectrum of the NO-released species revealed *g* values of 2.23, 2.03, and 2.02, indicating the formation of low-spin $[Fe^{III}(Cl_2PhPep\{SO_2\}_2)(DMAP)_2]^-$.

The first temperature-dependant spin-crossover photoactive complex, $[Fe(N3PyS)(NO)]^+$ (**13**), was reported, utilizing a tetradentate N3S ligand (Chart 1k).[48,49] Complex **13** was synthesized by reacting $[Fe^{II}(N3PyS)(CH_3CN)]^+$ with NO gas. X-ray diffraction revealed a distorted octahedral geometry for **13** with the NO ligand positioned *trans* to the amine nitrogen in the axial position (Fig. 2c). Magnetic susceptibility experiments indicated that **13** exhibited a low-spin ($S = 1/2$) state within the temperature range of 10–150 K, while an increasing contribution of a high-spin ($S = 3/2$) state was observed above 150 K. The spin-crossover of **13** resulted in changes to the geometric parameters for bond lengths and NO stretching vibration energies at different temperatures. For the $S = 1/2$ state at 110 K, the bond distances of Fe–NO and N–O bond were 1.7327 and 1.150 Å, respectively. In contrast, at 293 K, the Fe–NO and N–O bond lengths were determined to be 1.747 and 1.14 Å, respectively (Table 2). The ATR-IR spectrum of crystalline **13** at room temperature displayed two NO stretching bands at 1753 and 1660 cm^{-1}, indicative of a mixture of $S = 3/2$ and $S = 1/2$ species. Upon $^{15}N^{18}O$ labelling, NO vibrational frequencies shifted to lower energies of 1677 and 1587 cm^{-1}.

The release of NO from **13** was triggered by photoillumination with visible light ($\lambda > 400$ nm, 150 W) in CH_3CN. The photorelease led to the clean conversion of **13** to the NO-released species, $[Fe^{II}(N3PyS)(CH_3CN)]^+$, as evidenced by UV-vis spectral changes with an isosbestic point at 380 nm. Upon light irradiation, the characteristic absorption band of **13** at 360 nm decreased, while the bands at 418 and 493 nm, corresponding to the photoproduct, increased.

The photoactive Fe–NO complex, $[Fe(N3PyS)(NO)]^{2+}$ (**14**), was prepared through an one-electron oxidation of the $\{FeNO\}^7$ complex **13**.[50] The oxidation reaction was initiated by adding one equivalent of acetylferrocenium tetrafluoroborate ($AcFcBF_4$) to a solution of **13**, resulting in the appearance of new UV-vis absorption bands at 342 and 636 nm (Scheme 4). Similar results were observed with other oxidants such as tris(4-bromophenyl)ammoniumyl tetrafluoroborate and thianthrenium tetrafluoroborate. Complex **14** was unstable in CH_3CN at 25 °C, decomposing within minutes. However, the stability was significantly improved when oxidation was performed at a lower temperature of −40 °C, extending the lifetime up to 8 hours. Stability was also enhanced in the non-coordinating solvent CH_2Cl_2, where **14** remained stable at 25 °C for 24 hours without noticeable decomposition.

Although the crystal structure of **14** could not be obtained, extended X-ray absorption fine structure (EXAFS) analysis provided an Fe–NO bond length of 1.69 Å. The IR spectrum of **14** showed an NO vibrational band at 1909 cm^{-1}, which aligns with typical values for $\{FeNO\}^6$ complexes. The Mössbauer spectrum at 80 K displayed an isomer shift (δ) value of 0.03 mm s^{-1} and quadrupole splitting (ΔE_Q) of 1.7 mm s^{-1}, consistent with a Fe^{II}–NO^+ configuration. The Mössbauer parameters are similar to those of the NO-bound Fe-NHase enzyme (δ = 0.03 mm s^{-1} and $\Delta E_Q = 1.47$ mm s^{-1}).

Photorelease of NO from **14** was observed upon exposure to visible light ($\lambda > 400$ nm) in CH_3CN at −40 °C, resulting in the rapid decomposition into the $[Fe^{III}(N3PyS)(CH_3CN)]^{2+}$ precursor complex. However, irradiation of **14** in CH_2Cl_2 at both 25 and −40 °C did not lead to NO release, likely due to the rapid rebinding of NO in the non-coordinating solvent.

A photo-sensitive complex, $[Fe((CH_2Py_2)_2Me[9]aneN_3)(NO)]^{2+}$ (**15**), was synthesized using a pentadentate N5 ligand (Chart 1n).[51] The synthesis of **15** was achieved in a single step by

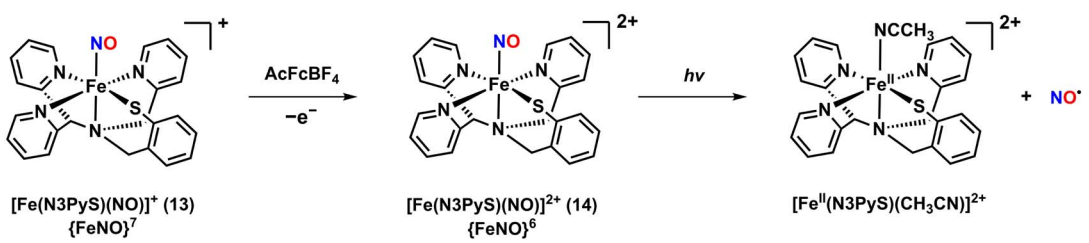

Scheme 4 Generation of the $\{FeNO\}^6$ complex **14** by one-electron oxidation from the $\{FeNO\}^7$ complex **13**.

bubbling NO gas into a solution of CH_3CN/MeOH mixture containing $Fe(BF_4)_2 \cdot 5H_2O$ and the $(CH_2Py_2)_2Me[9]aneN_3$ ligand, resulting in the generation of black solution of **15**. Crystals suitable for X-ray diffraction analysis were obtained through slow evaporation of the resulting solution under an Ar stream. The X-ray diffraction revealed Fe–NO and N–O bond distances of 1.731 and 1.143 Å, respectively, with a bent Fe–N–O angle of 148.3°. The X-band EPR spectrum of **15** in frozen CH_3CN at 30 K exhibited a rhombic signal at g value of 2.00 with hyperfine splitting due to the interaction of the Fe center with the ^{14}N nucleus of the ligand donor atom, indicative of an $S = 1/2$ spin state. The IR spectrum showed a strong NO stretching peak at 1660 cm^{-1}, typical for low-spin $\{FeNO\}^7$ complexes.

The photodissociation of **15** in CH_3CN resulted in the release of NO with a quantum yield of 0.52 upon exposure to a 450 nm light source. A lower quantum yield of 0.40 was observed with 365 nm light in CH_3CN. The isosbestic point in the UV-vis spectrum indicated a complete conversion to the solvent-bound Fe(II) starting complex, $[Fe^{II}((CH_2Py_2)_2Me[9]aneN_3)(CH_3CN)]^{2+}$. The released NO was qualitatively detected by reacting NO with reduced myoglobin (Mb) that is prepared by reducing metMb with sodium dithionite. The free NO radical was transferred by an Ar stream to the metMb solution, and the spectral change in the UV-vis spectrum due to NO coordinating to the Fe(II) center of Mb was monitored.

Two photolabile complexes, $[Fe(^{TMS}PS2)(^{TMS}PS2H)(NO)]$ (**16**) and $[Fe(^{TMS}PS2)(^{TMS}PS2CH_3)(NO)]$ (**17**), bearing a pendant thiol and thioether (Chart 1l), respectively, were reported.[52] The neutral complex **16** was synthesized by treating $Fe(CO)_2(NO)_2$ in THF with two equivalents of the $^{TMS}PS2H_2$ ligand in the absence of light. Complex **17** was produced by methylating the pendant thiol of **16** with trimethyloxonium tetrafluoroborate (Me_3OBF_4), resulting in a thioether as shown in Scheme 5. X-ray crystallography revealed that both complexes feature Fe coordination environments with two phosphine donors in the axial position and three thiolate and one NO in the equatorial plane, resulting in distorted octahedral geometries. The Fe–NO and N–O bond distances were nearly identical for both complexes (Fe–NO = 1.644 Å for **16** and 1.642 Å for **17**; N–O = 1.153 Å for **16** and 1.152 Å for **17**). The IR spectra showed NO stretching bands at 1829 cm^{-1} for **16** and 1822 cm^{-1} for **17**, which were sensitive to the ^{15}NO isotope. The diamagnetic signals of ^1H NMR indicated $S = 0$ ground states for **16** and **17**.

As illustrated in Scheme 5, photolysis (λ > 400 nm, 150 W, xenon lamp) of **16** in toluene at ambient temperature for 20 seconds led to the formation of a unique intermediate involving an intramolecular [SH···ON–Fe] interaction between NO and a pendant SH group within the ligand framework. The intramolecular interaction was evidenced by an IR band shift of the NO stretching frequency from 1833 to 1823 cm^{-1} and a downfield shift from 4.79 to 5.78 ppm of ^1H NMR for the proton on the pendent SH group, attributable to the hydrogen bonding interaction.[57–60] Prolonged irradiation led to a decrease in the intensity of the NO vibration peak at 1823 cm^{-1}, indicating partial NO loss, along with the appearance of IR bands at 2219 and 1774 cm^{-1} corresponding to the formation of N_2O and

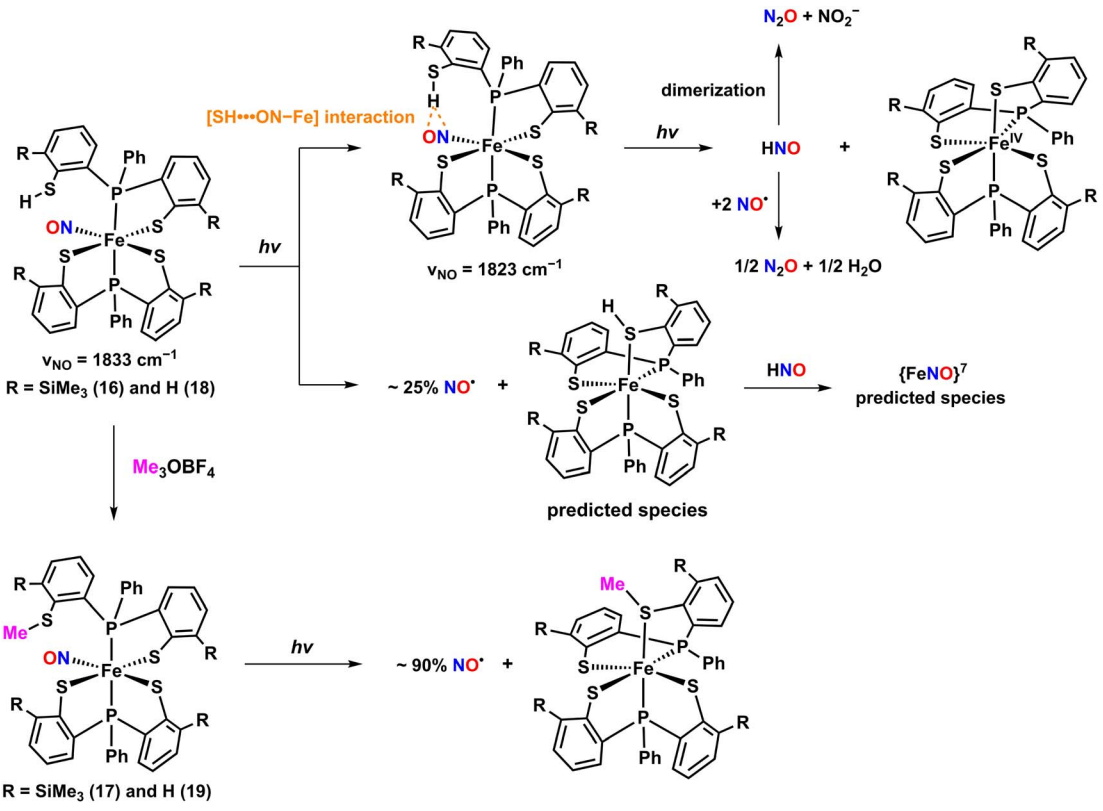

Scheme 5 Proposed photolysis pathways of complexes **16**–**19**.

predicted $\{FeNO\}^7$ species, respectively. The generation of N_2O implies that HNO was initially formed through proton-coupled electron transfer reaction *via* the [SH···ON–Fe] interaction,[61–63] which then either dimerized or reacted with partially released NO to form N_2O. The release of NO was further confirmed by the formation of [Co(TPP)(NO)] adduct from [Co(TPP)] and N_2O was characterized by gas chromatography (GC) analysis. The photoproduct of **16** was crystallized and characterized by SC-XRD and Mössbauer spectroscopy (δ = 0.15 mm s^{-1}, ΔE_Q = 1.99 mm s^{-1}, and Γ = 0.29 mm s^{-1}) to be an intermediate spin state of $S = 1$ Fe(IV) species. In contrast, the photolysis of **17** resulted only in NO release. The absence of a pendant SH group in **17** prevented the formation of the [SH···ON–Fe] intermediate, which played a crucial role in the HNO production pathway seen in **16**.

Additional photolabile complexes, [Fe(PS2)(PS2H)(NO)] (**18**) and [Fe(PS2)(PS2CH_3)(NO)] (**19**), were reported as analogous to complexes **16** and **17**.[53] Complexes **18** and **19** were prepared using the same methodology employed for **16** and **17** (Chart 1m). The both complexes exhibited distorted octahedral geometries similar to those of **16** and **17**, with nearly linear bond angles of Fe–N–O units (175.56° for **18** and 175.05° for **19**). The Fe–NO and N–O bond lengths in **18** were measured to be 1.6513 and 1.152 Å, respectively, while in **19**, they were slightly shorter at 1.6449 and 1.150 Å. The ^{1}H NMR spectra of both complexes indicated diamagnetic signals, suggesting low-spin $\{FeNO\}^6$ complexes.

A solution IR study of NO photodissociation from **18** under xenon lamp irradiation (λ > 400 nm, 150 W) in CH_2Cl_2 at room temperature revealed a notable decay of the NO stretching peak at 1836 cm^{-1}, accompanied by the appearance of a 2223 cm^{-1} band corresponding to N_2O formation. The IR band change was similar to that observed in **16**, indicating HNO formation through an intramolecular [SH···ON–Fe] interaction between NO and a pendant SH group. In contrast, like **17**, **19** exhibited NO release under the same light conditions, evidenced by a decrease of the NO stretching band at 1823 cm^{-1}. The UV-vis spectroscopy was also used to monitor the photolysis of **18** and **19**. Upon photoillumination of **18**, the UV-vis bands at 500, 570, 665, and 915 nm gradually increased, indicating that **18** is photo-sensitive to forming NO and HNO under visible light. The UV-vis absorption bands were reminiscent of photoproduct of **16** (475, 535, 670, and 865 nm), suggesting the formation of [Fe(PS2)$_2$] as a photo-induced product. Likewise, for complex **19**, the UV-vis spectra showed growth of bands at 480, 560, 705, and 885 nm comparable to the photoproduct of **17** with bands at 470, 540, 700, and 865 nm, indicating the formation of NO-released species, [Fe(PS2)(PS2CH_3)].

A Fe–NO complex, $[Fe(TBDAP)(NO)(H_2O)]^{2+}$ (**20**), which contains a tetradentate N4 macrocyclic ligand (Chart 1p) was recently reported.[54] Complex **20** was synthesized by reacting an excess of NO gas with a CH_3CN solution of the Fe(II) precursor complex, $[Fe^{II}(TBDAP)(CH_3CN)_2]^{2+}$. Crystallographic analysis of **20** revealed a distorted octahedral geometry with NO and H_2O ligands coordinated to the Fe center at *cis* positions (Fig. 2e). The N–O and Fe–NO bond lengths were measured to be 1.153 and 1.754 Å, respectively, while the Fe–N–O angle was bent at 152.9°. The ATR-IR spectrum of crystalline **20** showed a NO stretching band at 1781 cm^{-1}. To determine the electronic configuration of **20**, ^{1}H NMR Evans method and X-band EPR analysis were performed. The effective magnetic moment was found to be 4.31 μ_B, and the EPR spectrum in a frozen acetone at 5 K displayed g values of 4.28, 3.79, and 1.99, indicating an Fe^{III}–NO^- ($S = 3/2$) states with antiferromagnetic coupling between high-spin Fe^{III} ($S = 5/2$) and NO^- ($S = 1$). The CASSCF calculations on the electronic structure of **20** in the ground state also suggested that 5.46 electrons occupy the five d-orbitals of the Fe center, and 1.71 electrons occupy the two π*-orbitals of the NO ligand, representing an Fe^{III}–NO^- state.

The photodissociation reaction of an aqueous solution of **20** at 37 °C resulted in the release of NO with a quantum yield of 0.23 under the white light irradiation (λ_{irr} = 385–740 nm, 300 W, xenon lamp) (Table 3). The characteristic UV-vis absorption bands at 407, 522, and 745 nm disappeared upon illumination, resulting in the Fe(II) precursor species. The released NO was captured by [Co(TPP)], resulting in [Co(TPP)(NO)], which was confirmed by characteristic UV-vis absorption bands at 414 and 538 nm. The generation of the Fe(II) complex was further supported by electrospray ionization mass (ESI-MS) spectrometry. Additionally, the total amount of released free NO was quantified to be 0.90 using the Griess assay.

2.4 Cobalt–nitrosyl complexes

The photo-sensitive complex, $[Co(MDAP)(NO)(CH_3CN)]^{2+}$ (**21**), with a tetradentate N4 macrocyclic ligand (Chart 1o), was synthesized by exposing NO gas to a CH_3CN solution of $[Co^{II}(MDAP)(CH_3CN)_2]^{2+}$ at −40 °C.[55] Complex **21** exhibited UV-vis absorption bands at 330 and 480 nm in CH_3CN. The X-ray crystal structure of **21** revealed that the coordination environment consists of four nitrogen atoms from the macrocyclic MDAP ligand, one nitrogen from CH_3CN, and one nitrogen from NO, forming a distorted octahedral geometry (Fig. 3). The Co–NO and N–O bond lengths were measured to be 1.855 and 1.097 Å, respectively, and the Co–N–O unit had a significant bending angle of 125.2°. The IR spectrum of **21** showed a NO stretching vibration at 1634 cm^{-1}, consistent with previously reported $\{CoNO\}^8$ complexes. The ^{1}H NMR signal of **21** was observed in the range of 0–10 ppm, indicating a diamagnetic low-spin $\{CoNO\}^8$ ground state.

In an aerobic aqueous solution, **21** demonstrated minimal NO release under dark conditions for 30 minutes. However, when the aqueous solution of **21** was exposed to white light (xenon lamp, λ_{irr} = 385–740 nm, 300 W), significant changes

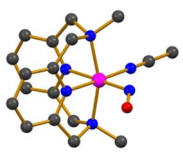

Fig. 3 Crystal structure of the Co–NO complex, $[Co(MDAP)(NO)(CH_3CN)]^{2+}$ (**21**) (dark grey, C; blue, N; red, O; magenta, Co).

were observed, particularly a decrease in the absorption band at 330 nm. NO was rapidly photo-released from **21**, with a half-life of 12 seconds, following first-order kinetics. The quantum yield for photo-released NO was calculated to be 0.78 using standard ferrioxalate actinometry (Table 3). In CH_3CN, NO photolysis process was even faster, with a half-life of 6 seconds, also following first-order kinetics. The released NO was captured by [Co(TPP)], forming [Co(TPP)(NO)], confirmed by characteristic UV-vis absorption bands of at 414 and 538 nm. The final product after photolysis was identified as the $[Co^{II}(MDAP)(CH_3CN)_2]^{2+}$ precursor complex. The Griess assay further confirmed the photo-induced release of NO.

3. Discussion

3.1 Ligand effect

The design of supporting ligands plays a critical role in modulating the photoactivity of nitrosyl complexes, which is particularly important for potential biological applications, such as controlled NO release. Ligands can significantly influence the electronic structure, absorption properties, and photoreactivity. By introducing functional groups with various electronic properties, such as extended conjugation or electron-donating and electron-withdrawing substituents, the photolability and overall behavior of nitrosyl complexes can be fine-tuned. The effects of ligands on photolability have been experimentally and theoretically examined.

3.1.1 Conjugation effect. The role of ligand conjugation on the photolability of $\{MnNO\}^6$ complexes **1–4** has been explored through detailed characterization and photoreactivity studies.[36–38] The investigation highlights how changes in the ligand backbone, specifically through the introduction of extended conjugation, lead to enhanced photosensitivity at longer wavelengths. In complexes **1** and **2**, the pyridyl-carboxamide group in **1** (Chart 1a) was replaced with a quinolyl-carboxamide moiety in **2** (Chart 1b). The substitution increased the conjugation in the ligand, resulting in a red-shift in absorption bands from 635 nm for **1** to 670 nm for **2**. Similarly, for the Schiff base nitrosyl complexes **3** and **4**, replacing the pyridyl-imine group in **3** (Chart 1c) with the quinolyl-imine moiety in **4** (Chart 1d), spectroscopic features were observed with a shift from 720 to 785 nm due to the increased conjugation in the ligand framework.

Time-dependent density functional theory (TD-DFT) calculations further provided insight into the effects of conjugation on the red-shift of light responsiveness.[64] Computational results elucidated that the level of the lowest unoccupied molecular orbital (LUMO) in **2** is significantly lower than that of **1** due to energy stabilization by the extended conjugation of the quinoline group. A comparable effect was also observed in **3** and **4**. However, the highest occupied molecular orbital (HOMO) levels showed only slight changes (Fig. 4). These results indicated that quinoline substitution notably impacts the LUMO levels of **2** and **4**, leading to narrower energy gaps between HOMO and LUMO, which are associated with electronic transitions. Consequently, smaller energy differences between HOMO and LUMO levels induce electronic excitation at lower energy, resulting in the red-shifted UV-vis absorption bands observed in **2** and **4**.

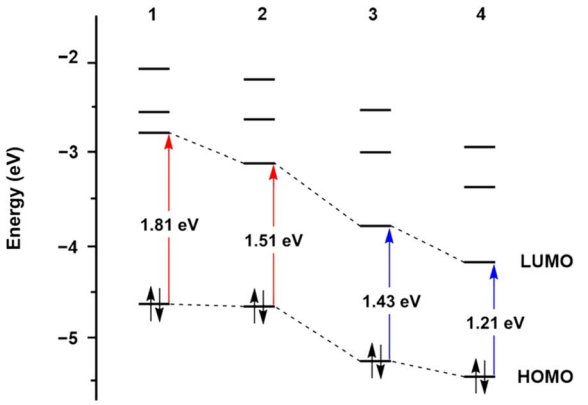

Fig. 4 Time-dependent density functional theory (TD-DFT) results showing the molecular orbital energy levels for complexes **1–4**.

3.1.2 Electronic effect. The introduction of electron-donating and -withdrawing substituent groups into supporting ligands is an effective strategy to fine-tune the electronic properties of metal–nitrosyl complexes, which in turn impacts the photoreactivity. In a study by Hitomi and co-workers, both electron-withdrawing and electron-donating groups were incorporated into manganese nitrosyl complexes to explore electronic effects.

As shown in Chart 1e, the electrochemical properties of the H-dpaq^R ligand (R = OCH_3, H, Cl, and NO_2) were systematically altered.[39] The cyclic voltammograms of all the complexes exhibited quasi-reversible behavior associated with the $\{MnNO\}^{5/6}$ redox couple. The redox potentials ($E_{1/2}$ *vs.* Fc^+/Fc) showed a linear trend in the order of $\mathbf{5}^{NO_2}$ (0.63 V) > $\mathbf{5}^{Cl}$ (0.56 V) > $\mathbf{5}^{H}$ (0.52 V) > $\mathbf{5}^{OMe}$ (0.49 V). The increase in redox potentials with stronger electron-withdrawing substituents indicates that π-backdonation from the Mn center to the NO ligand decreases as the electron density at the Mn center diminishes. In IR spectroscopy, the NO stretching frequencies shifted to higher energies with electron-withdrawing groups. The shift signifies a reduction in π-backdonation from Mn to NO, weakening the bond between Mn and the NO ligand.

The electronic effects also influenced the UV-vis absorption spectra of the complexes. As the electron-withdrawing character of the substituents increased, the absorption bands of the nitrosyl complexes exhibited a red-shift (Table 1). Notably, the $\mathbf{5}^{NO_2}$ complex displayed a distinctive absorption profile with an extended tail into the NIR region up to 700 nm due to the stabilization of the quinoline π* orbitals by the nitro group. The observed shifts in absorption bands induced by the electronic nature of substituent groups significantly affected the photolysis rates of the nitrosyl complexes under different light conditions.

As shown in Table 4, the rate constants for photolysis decreased with electron-withdrawing substituents under 460 nm light, indicating a slower NO release. However, under longer wavelength light exposure at 530 and 650 nm, the

Table 4 Extinction coefficients and initial rate constant of the NO release

	Extinction coefficients [mM^{-1} cm^{-1}]			Rate constant [μM s^{-1}]		
Complex	460 nm	530 nm	650 nm	460 nm	530 nm	650 nm
$\mathbf{5}^{OMe}$	4.20	0.370	0.111	1.17	0.254	0.0835
$\mathbf{5}^{H}$	3.11	0.363	0.123	1.79	0.300	0.0999
$\mathbf{5}^{Cl}$	2.69	0.707	0.113	1.26	0.494	0.0988
$\mathbf{5}^{NO_2}$	1.77	1.56	0.493	0.84	0.809	0.252

opposite trend was observed. Remarkably, the photolysis rate of $\mathbf{5}^{NO_2}$ was significantly enhanced under 650 nm light compared to the other derivatives. The enhancement is attributed to the extended absorption band into the NIR region. Consequently, the electronic effects of the substituent groups on supporting ligands can modulate the UV-vis absorption bands, and the changes in UV-vis features alter light absorptivity at specific wavelengths, which in turn affects the rate of NO release.

3.2 Computational studies on photodissociation mechanisms

3.2.1 Ligand-to-metal charge transfer (LMCT). Computational studies including time-dependent density functional theory (TD-DFT) have provided valuable insight into the electronic transitions responsible for the photodissociation of nitrosyl complexes. The photolability of Fe–NO complexes, such as **8** and **12**, has been attributed to ligand-to-metal charge transfer (LMCT). For **8**, the lowest energy transition by 480 nm arises from a nb(amide) + d_π(Fe)–π(NO) → d_π(Fe)–π*(NO) transition, weakening the Fe–NO bond. Another electronic transition at 337 nm involves a nb(amide) + d_{xy}(Fe) → d_π(Fe)–π*(NO) transition, which also facilitates NO release.[65,66] In **12**, transitions at 707 and 743 nm originate from the d_{xy}(Fe) + L(amide) → d_{z^2}(Fe)–σ*(NO) and a L(amide/SO_2) → d_π(Fe)–π*(NO) transitions, respectively.[65] The transitions observed in **8** and **12** involve electronic transitions from bonding orbitals to antibonding orbitals. Thus, the TD-DFT calculations clearly demonstrate that the electronic transitions from ligand-dominated molecular orbitals to Fe–NO antibonding orbitals significantly weaken the Fe–NO bond, thereby increasing the probability of photodissociation.

3.2.2 Metal-to-ligand charge transfer (MLCT). For Mn–NO complexes **1** and **2**, metal-to-ligand charge transfer (MLCT) was identified as the dominant photodissociation mechanism by Lehnert *et al.*[67] According to TD-DFT results, light irradiation in the UV region for **1** and **2** leads to NO-release through transitions such as L(amide) + d_π(Mn)–π(NO) → nb(Py) + d_π(Mn)–π*(NO) and d_π(Mn)–π(NO) → d_π(Mn)–π*(NO). The excitations involve transitions from the Mn–NO bonding to Mn–NO antibonding orbitals *via* MLCT. Further MLCT transitions of nb(amide) + d_π(Mn)–π(NO) → nb(Py) + d_π(Mn)–π*(NO) by 450–500 nm also promote NO photorelease. Interestingly, NO release by NIR light follows a different excitation mechanism involving intersystem crossing (IC). Initially, a MLCT of d_{xy}(Mn) → L(amido) transition occurs, followed by interconversion into the d_{xy}(Mn) → d_π(Mn)–π*(NO) state (T1). Finally, the T1 state decays *via* Mn–NO bond dissociation.

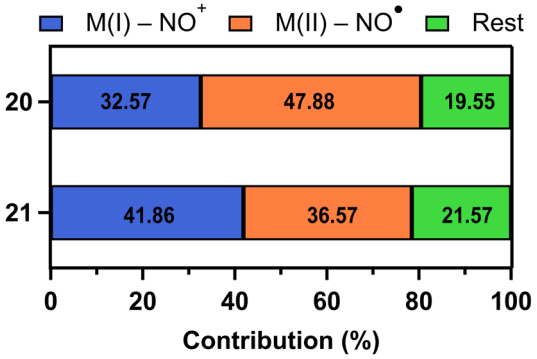

Fig. 5 Bar graphs highlight the M^{I}–NO^{+} configuration percentage of complexes **20** and **21** involved in reaching the MLCT state.

To further elucidate the mechanism of photodissociation in iron and cobalt nitrosyl complexes, complete active space self-consistent field (CASSCF) calculations were performed on **20** and **21**.[54] For **20**, the CASSCF results suggested a resonance between Fe^{I}–NO^{+}, Fe^{II}–$NO^{\bullet}$, and Fe^{III}–NO^{-} configurations in the ground state, with Fe^{III}–NO^{-} being the dominant form. The low-lying excited states Q_1 and Q_2 were mainly composed of the Fe^{II}–$NO^{\bullet}$ state, which can be accessed *via* metal-to-ligand charge transfer (MLCT) from the Fe^{I}–NO^{+} configuration at 740 nm. The transitions involve electron transfer from Fe-dominated Fe–NO bonding orbitals to NO-π*-dominated Fe–NO antibonding orbitals, leading to Fe–NO bond cleavage and the release of NO.

Similarly, in **21**, the CASSCF results indicated that the absorption band at 480 nm is associated with an MLCT transition from Co^{I}–NO^{+} to Co^{II}–$NO^{\bullet}$ configuration, resulting in NO photodissociation. Notably, **21** is more likely to reach the MLCT than **20** because the contribution of M^{I}–NO^{+} state to MLCT showed higher probability (41.86% for **21** and 32.57% for **20**) (Fig. 5). These probabilities indicate the likelihood of undergoing MLCT. Due to the higher percentage for complex **21**, it has a greater quantum yield (0.78 for **21** *versus* 0.23 for **20**) and a faster photolysis rate with a half-life of 24 seconds for **21** compared to 255 seconds for **20**.

3.3 Structural and spectroscopic correlations in the Fe–N–O unit

The relationships between structural and spectroscopic properties offer valuable insights into the electronic structures of transition metal complexes. In metal–carbonyl (M–CO) complexes, there are well-established correlations between C–O bond length and stretching frequency. Additionally, the inverse relationship between M–CO bond and C–O bond distance, caused by π-backdonation, is widely accepted.[68–70]

Similarly, in nitrosyl complexes, the bonding between the metal and NO involves a combination of σ-donation from NO to the metal and π-backdonation from the metal to the NO-π* orbital. Complexes with linear bond angles (170–180°) are considered more capable of donating electron density from the metal to the NO-π* orbital. In contrast, complexes with bent

angles (120–170°) are more restricted to provide electron density through π-backdonation.[71] Despite numerous studies on nitrosyl complexes based on the general understanding, the structural and spectroscopic relationships in M–NO complexes often display irregularities that challenge conventional expectations.[72]

In Mn–NO species, to validate the correlation between NO stretching vibration energies and N–O bond lengths, $\{MnNO\}^6$ complexes supported by anionic pentadentate N5 carboxamide ligands that can provide comparable coordination environments were plotted. Only complexes with the same spin state ($S = 0$) and a linear bond angle (170–180°) were considered.[36–39] However, as shown in Fig. 6a, no linear correlation was observed between the vibrational energy and N–O bond strength. Additionally, the plot of the relationship between N–O bond length and Mn–NO distance also indicated no clear correlation (Fig. 6b). In contrast, for $S = 0$ $\{FeNO\}^6$ complexes, a correlation between NO stretching vibration energies and N–O bond lengths follows the expected trend where the IR frequency increases as the N–O bond shortens, although the coordination environments are not considered.[41–45,52,53] Moreover, the N–O bond length decreases when the Fe–NO bond weakens, demonstrating the influence of π-backdonation in the Fe–N–O unit.

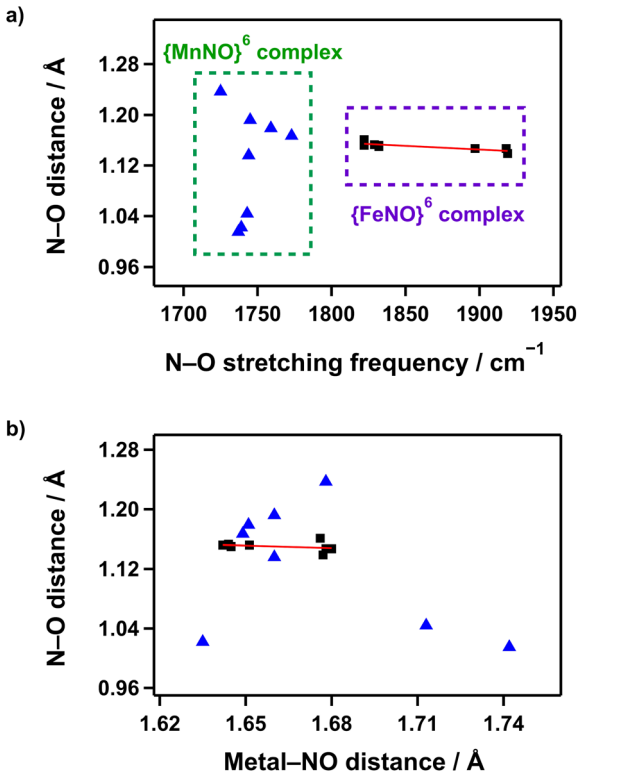

Fig. 6 (a) Plot of the N–O bond distance (Å) against the N–O bond stretching frequency (cm^{-1}) for $\{MnNO\}^6$ and $\{FeNO\}^6$ complexes. (b) Plot of the N–O bond distance (Å) against the M–NO bond length (Å). Triangle (blue) and rectangle (black) represent $\{MnNO\}^6$ and $\{FeNO\}^6$ complexes, respectively. The solid red line shows a least-squares linear fit of the data.

Overall, the structural and spectroscopic relationships in the M–N–O unit remain challenging to fully understand. The irregularities observed in Mn–NO and Fe–NO complexes suggest that the bonding interactions between metal and NO are highly sensitive to metal identity, coordination geometry, and environmental factors. Further systematic and comprehensive investigations are necessary to clarify the relationships and develop a more complete understanding of the underlying principles governing metal–nitrosyl chemistry.

4. Application

4.1 Vasodilation and reperfusion

Endogenously produced NO plays an essential role in vascular regulation. NO diffuses into smooth muscle cells and stimulates the conversion of guanosine-5′-triphosphate (GTP) into cyclic guanosine-3′,5′-monophosphate (cGMP) through the activation of the soluble guanylyl cyclase (sGC) enzyme. Elevated cGMP levels trigger the activation of protein kinase G (PKG), leading to the subsequent activation of extracellular signal-regulated kinases (ERKs). The cascade ultimately promotes vasodilation through the relaxation of smooth muscle cells.[8,9]

Mascharak and co-workers demonstrated the potential of a photo-responsive Mn–NO complex **1** to induce vasodilation. Under light irradiation, **1** dramatically increases sGC activation in physiological environment. In rat aorta smooth muscle cells, **1** triggered vasorelaxation when exposed to visible light.[73] The vasodilatory effect was reduced by the sGC inhibitor, 1*H*-[1,2,4]oxadiazolo[4,3-*a*]quinoxalin-1-one (ODQ), supporting that **1** can effectively activate sGC in the presence of light.

Cho and co-workers showed that ERK pathways in live cells can be selectively activated through light-triggered NO delivery using Co–NO complex **21**, revealing distinct kinetic differences between endogenous and exogenous NO delivery.[55] A kinase translocation reporter (KTR) cell line was developed to visualize the ERK signaling pathway in real-time, enabling quantitative comparison of endogenous and exogenous NO delivery on ERK activation. Additionally, the study confirmed that NO-induced ERK activation did not result from non-specific perturbation of membrane receptors, including the epidermal growth factor receptor (EGFR), validating that NO regulates ERK signaling with distinct dynamics based on spatial regions at the single-cell levels.

Furthermore, the therapeutic potential of the Fe–NO (**20**) and Co–NO (**21**) complexes for retinal vascular occlusion (RVO), a disease that impairs blood flow in the retina, was investigated.[54] **20** and **21** were intravitreally injected into the eyes of mice with transient light exposure, resulting in significant dilation of retinal blood vessels. Notably, in the artificially induced mouse RVO model, only complex **20** rapidly opened occluded sites and successfully facilitated reperfusion. The research speculated that the superior therapeutic effect of complex **20** can be attributed to the relatively slow photoresponse, resulting in a sustained NO release that effectively induces vasodilation and reperfusion. Additionally, NO-releasing donors such as diethylenetriamine diazeniumdiolate

(DETA-NONOate) and sodium nitroprusside (SNP) were employed under identical conditions as positive controls. For DETA-NONOate and SNP, however, adverse effects like exudative retinal detachment occurred 10 minutes after injection. These findings suggest that the treatment strategy using M–NO with light exposure can be extended to effectively treat other vascular diseases.

4.2 Immune response and antibiotic effect

NO is a powerful bioactive molecule that plays a multifaceted role in immune system, by interacting with transition metal ions or reactive oxygen species (ROS), including superoxide, peroxide, and dioxygen, to form reactive nitrogen species (RNS) such as peroxynitrite ($ONOO^-$) and nitrogen dioxide (NO_2). The RNS exerts nitrosative stress on pathogen, targeting DNA, proteins, and lipids, which helps eradicate invading bacteria and enhances the body's defense mechanism.[74]

To harness NO's antimicrobial properties, light-responsive NO delivery systems targeting drug-resistant bacteria was employed.[73,75,76] One such system incorporated **1** into a sol–gel matrix that allowed precise NO release under visible light, which effectively reduced bacterial loads of *Pseudomonas aeruginosa* (*P. aeruginosa*, Gram-negative), *Escherichia coli* (*E. Coli*, Gram-negative), *Staphylococcus aureus* (*S. aureus*, Gram-positive), and methicillin-resistant *Staphylococcus aureus* (MRSA, antibiotic-resistant). This approach demonstrated the potential for localized treatment of infections, offering a significant advantage over conventional antibiotic treatment.

The polyurethane-based composite (PUX-NO) films with embedded NO-releasing silica particles containing **1** was developed.[77] The films exhibited high stability and capacity of NO release over extended periods, which is suitable for applications as wound dressings. The PUX-NO films showed effective reduction of bacterial loads of both Gram-positive and Gram-negative bacteria, including MRSA and *S. aureus*, under controlled light exposure, indicating the potential for treatment of skin and soft-tissue infections (SSTI).

A porous material MCM-41 loading complex **1** was developed to eradicate the drug-resistant bacterium *Acinetobacter baumannii* (*A. baumannii*), which exhibits a high transmission rate of infection in hospital settings.[78] The loading efficiency was confirmed by using powder X-ray diffraction (PXRD) and N_2 adsorption/desorption isometry. In the absence of visible light, the material demonstrated significant stability with minimal leaching of **1** in physiological saline. Upon exposure to low-power (10–100 mW) visible light, rapid NO release was observed while the photoproducts were retained within the host structure, decreasing the risk of toxicity from the material. This strategy reveals the potential of photo-triggered NO delivery systems for effective treatment of multidrug-resistant bacterial infections in challenging clinical environments.

5. Conclusions and outlook

In this review, we have summarized the recent progress in the development of photo-triggered NO release from first-low transition metal–nitrosyl complexes, focusing on the geometric and electronic structures that determine photoreactivity and NO release efficiency. Key advancements have emerged from the modulation of ligand frameworks through the introduction of π-conjugation systems and electronic substituents, allowing for more precise control over light responsiveness. The modifications have enhanced the potential of nitrosyl complexes for biomedical applications. Spectroscopic and computational studies have provided crucial insights into the mechanisms of photodissociation, revealing that the electronic transitions from bonding to antibonding orbitals play a pivotal role in facilitating NO release.

Despite advancements, several challenges remain. One of the most significant barriers to clinical application is optimizing key photophysical properties such as quantum yield and activation wavelengths. To overcome obstacles, future research must focus on developing ligand frameworks that improve light absorption in the NIR region, enhance stability under physiological conditions, and minimize toxicity. The integration of experimental results with computational modeling is also essential to predict and refine photoreactivity, enabling the development of more effective NO donors. Such innovations could significantly broaden the therapeutic potential of nitrosyl complexes, enabling their use in a wider range of medical applications such as cardiovascular disease treatment and targeted eradication of bacterial infections. Photo-responsive NO donors may become a key tool in advanced therapeutic strategies, offering precise control over NO delivery with minimal side effects.

Data availability

No primary research results, software or code have been included and no new data were generated or analysed as part of this review.

Author contributions

S. S. and J. Ce. wrote the manuscript. J. C. revised and supervised the manuscript.

Conflicts of interest

There are no conflicts to declare.

Acknowledgements

The research was supported by National Research Foundation funded by the Ministry of Science, ICT and Future Planning (RS-2024-00333606) and the Ministry of Health and Welfare (RS-2023-00217242) of Korea.

References

1 R. M. J. Palmer, A. G. Ferrige and S. Moncada, *Nature*, 1987, **327**, 524–526.

2 C. Farah, L. Y. M. Michel and J.-L. Balligand, *Nat. Rev. Cardiol.*, 2018, **15**, 292–316.
3 E. Culotta and D. E. Koshland, *Science*, 1992, **258**, 1862–1865.
4 S. H. Snyder, *Science*, 1992, **257**, 494–496.
5 C. Bogdan, *Nat. Immunol.*, 2001, **2**, 907–916.
6 S. M. Andrabi, N. S. Sharma, A. Karan, S. M. S. Shahriar, B. Cordon, B. Ma and J. Xie, *Adv. Sci.*, 2023, **10**, 2303259.
7 M. A. Cinelli, H. T. Do, G. P. Miley and R. B. Silverman, *Med. Res. Rev.*, 2020, **40**, 158–189.
8 Y. Kang, R. Liu, J.-X. Wu and L. Chen, *Nature*, 2019, **574**, 206–210.
9 R. Liu, Y. Kang and L. Chen, *Nat. Commun.*, 2021, **12**, 5492.
10 I. Endo, M. Nojiri, M. Tsujimura, M. Nakasako, S. Nagashima, M. Yohda and M. Odaka, *J. Inorg. Biochem.*, 2001, **83**, 247–253.
11 I. Endo, M. Odaka and M. Yohda, *Trends Biotechnol.*, 1999, **17**, 244–248.
12 M. Odaka, K. Fujii, M. Hoshino, T. Noguchi, M. Tsujimura, S. Nagashima, M. Yohda, T. Nagamune, Y. Inoue and I. Endo, *J. Am. Chem. Soc.*, 1997, **119**, 3785–3791.
13 N. Lehnert, E. Kim, H. T. Dong, J. B. Harland, A. P. Hunt, E. C. Manickas, K. M. Oakley, J. Pham, G. C. Reed and V. S. Alfaro, *Chem. Rev.*, 2021, **121**, 14682–14905.
14 P. G. Wang, M. Xian, X. Tang, X. Wu, Z. Wen, T. Cai and A. J. Janczuk, *Chem. Rev.*, 2002, **102**, 1091–1134.
15 R. Scatena, P. Bottoni, G. Martorana and B. Giardina, *Expert Opin. Invest. Drugs*, 2005, **14**, 835–846.
16 D. A. Riccio and M. H. Schoenfisch, *Chem. Soc. Rev.*, 2012, **41**, 3731–3741.
17 J. A. Hrabie and L. K. Keefer, *Chem. Rev.*, 2002, **102**, 1135–1154.
18 V. N. Varu, N. D. Tsihlis and M. R. Kibbe, *Vascular and Endovascular Surgery*, 2009, **43**, 121–131.
19 J. Saraiva, S. S. Marotta-Oliveira, S. A. Cicillini, J. D. O. Eloy and J. M. Marchetti, *J. Drug Delivery*, 2011, **2011**, 936438.
20 S. Sortino, *Chem. Soc. Rev.*, 2010, **39**, 2903–2913.
21 P. G. Wang, M. Xian, X. Tang, X. Wu, Z. Wen, T. Cai and A. J. Janczuk, *Chem. Rev.*, 2002, **102**, 1091–1134.
22 R. Weinstain, T. Slanina, D. Kand and P. Klán, *Chem. Rev.*, 2020, **120**, 13135–13272.
23 H. M. Elbeheiry and M. Schulz, *Coord. Chem. Rev.*, 2024, **515**, 215921.
24 N. L. Fry and P. K. Mascharak, *Acc. Chem. Res.*, 2011, **44**, 289–298.
25 I. Stepanenko, M. Zalibera, D. Schaniel, J. Telser and V. B. Arion, *Dalton Trans.*, 2022, **51**, 5367–5393.
26 H.-J. Xiang, M. Guo and J.-G. Liu, *Eur. J. Inorg. Chem.*, 2017, **2017**, 1586–1595.
27 J. J. Becker, P. S. White and M. R. Gagné, *Inorg. Chem.*, 1999, **38**, 798–801.
28 I. Ara, J. Forniés, M. A. García-Monforte, B. Menjón, R. M. Sanz-Carrillo, M. Tomás, A. C. Tsipis and C. A. Tsipis, *Chem.–Eur. J.*, 2003, **9**, 4094–4105.
29 M. J. G. Sinclair, N. Roig, M. R. Gyton, N. Tsoureas, F. G. N. Cloke, M. Alonso and A. B. Chaplin, *Inorg. Chem.*, 2024, **63**, 1709–1713.
30 J. Xiang, Q. Wang, S.-M. Yiu, W.-L. Man, H.-K. Kwong and T.-C. Lau, *Inorg. Chem.*, 2016, **55**, 5056–5061.
31 J. Xiang, Q. Wang, S.-M. Yiu and T.-C. Lau, *Inorg. Chem.*, 2017, **56**, 2022–2028.
32 R. Bhowmik and M. Roy, *Eur. J. Med. Chem.*, 2024, **268**, 116217.
33 J. M. Mir, B. A. Malik and R. C. Maurya, *Rev. Inorg. Chem.*, 2019, **39**, 91–112.
34 M. J. Rose and P. K. Mascharak, *Curr. Opin. Chem. Biol.*, 2008, **12**, 238–244.
35 B. Heilman and P. K. Mascharak, *Philos. Trans. R. Soc., A*, 2013, **371**, 20120368.
36 K. Ghosh, A. A. Eroy-Reveles, B. Avila, T. R. Holman, M. M. Olmstead and P. K. Mascharak, *Inorg. Chem.*, 2004, **43**, 2988–2997.
37 A. A. Eroy-Reveles, Y. Leung, C. M. Beavers, M. M. Olmstead and P. K. Mascharak, *J. Am. Chem. Soc.*, 2008, **130**, 4447–4458.
38 C. G. Hoffman-Luca, A. A. Eroy-Reveles, J. Alvarenga and P. K. Mascharak, *Inorg. Chem.*, 2009, **48**, 9104–9111.
39 Y. Hitomi, Y. Iwamoto and M. Kodera, *Dalton Trans.*, 2014, **43**, 2161–2167.
40 Y. Iwamoto, M. Kodera and Y. Hitomi, *Chem. Commun.*, 2015, **51**, 9539–9542.
41 D. Schweitzer, J. J. Ellison, S. C. Shoner, S. Lovell and J. A. Kovacs, *J. Am. Chem. Soc.*, 1998, **120**, 10996–10997.
42 A. K. Patra, R. Afshar, M. M. Olmstead and P. K. Mascharak, *Angew. Chem., Int. Ed.*, 2002, **41**, 2512–2515.
43 A. K. Patra, J. M. Rowland, D. S. Marlin, E. Bill, M. M. Olmstead and P. K. Mascharak, *Inorg. Chem.*, 2003, **42**, 6812–6823.
44 R. K. Afshar, A. K. Patra, M. M. Olmstead and P. K. Mascharak, *Inorg. Chem.*, 2004, **43**, 5736–5743.
45 A. A. Eroy-Reveles, C. G. Hoffman-Luca and P. K. Mascharak, *Dalton Trans.*, 2007, 5268–5274.
46 M. J. Rose, N. M. Betterley and P. K. Mascharak, *J. Am. Chem. Soc.*, 2009, **131**, 8340–8341.
47 M. J. Rose, N. M. Betterley, A. G. Oliver and P. K. Mascharak, *Inorg. Chem.*, 2010, **49**, 1854–1864.
48 A. C. McQuilken, Y. Ha, K. D. Sutherlin, M. A. Siegler, K. O. Hodgson, B. Hedman, E. I. Solomon, G. N. L. Jameson and D. P. Goldberg, *J. Am. Chem. Soc.*, 2013, **135**, 14024–14027.
49 A. C. McQuilken, H. Matsumura, M. Dürr, A. M. Confer, J. P. Sheckelton, M. A. Siegler, T. M. McQueen, I. Ivanović-Burmazović, P. Moënne-Loccoz and D. P. Goldberg, *J. Am. Chem. Soc.*, 2016, **138**, 3107–3117.
50 A. Dey, A. M. Confer, A. C. Vilbert, P. Moënne-Loccoz, K. M. Lancaster and D. P. Goldberg, *Angew. Chem., Int. Ed.*, 2018, **57**, 13465–13469.
51 N. Levin, J. Perdoménico, E. Bill, T. Weyhermüller and L. D. Slep, *Dalton Trans.*, 2017, **46**, 16058–16064.
52 C.-K. Chiang, K.-T. Chu, C.-C. Lin, S.-R. Xie, Y.-C. Liu, S. Demeshko, G.-H. Lee, F. Meyer, M.-L. Tsai, M.-H. Chiang and C.-M. Lee, *J. Am. Chem. Soc.*, 2020, **142**, 8649–8661.
53 H.-C. Chen, G.-H. Lee, S.-Y. Chien and C.-M. Lee, *J. Chin. Chem. Soc.*, 2023, **70**, 1125–1135.

54 J. Choe, S. J. Kim, J.-H. Kim, M.-H. Baik, J. Lee and J. Cho, *Chem*, 2023, **9**, 1309–1317.
55 S. Shin, J. Choe, Y. Park, D. Jeong, H. Song, Y. You, D. Seo and J. Cho, *Angew. Chem., Int. Ed.*, 2019, **58**, 10126–10131.
56 J. H. Enemark and R. D. Feltham, *Coord. Chem. Rev.*, 1974, **13**, 339–406.
57 J. S. Southern, G. L. Hillhouse and A. L. Rheingold, *J. Am. Chem. Soc.*, 1997, **119**, 12406–12407.
58 R. Lin and P. J. Farmer, *J. Am. Chem. Soc.*, 2000, **122**, 2393–2394.
59 Y. Ling, C. Mills, R. Weber, L. Yang and Y. Zhang, *J. Am. Chem. Soc.*, 2010, **132**, 1583–1591.
60 E. G. Abucayon, R. L. Khade, D. R. Powell, Y. Zhang and G. B. Richter-Addo, *J. Am. Chem. Soc.*, 2016, **138**, 104–107.
61 S. A. Suarez, N. I. Neuman, M. Muñoz, L. a. Álvarez, D. E. Bikiel, C. D. Brondino, I. Ivanović-Burmazović, J. L. Miljkovic, M. R. Filipovic, M. A. Martí and F. Doctorovich, *J. Am. Chem. Soc.*, 2015, **137**, 4720–4727.
62 S. A. Suarez, M. Muñoz, L. Alvarez, M. F. Venâncio, W. R. Rocha, D. E. Bikiel, M. A. Marti and F. Doctorovich, *J. Am. Chem. Soc.*, 2017, **139**, 14483–14487.
63 I. Ivanovic-Burmazovic and M. R. Filipovic, *Inorg. Chem.*, 2019, **58**, 4039–4051.
64 W. Zheng, S. Wu, S. Zhao, Y. Geng, J. Jin, Z. Su and Q. Fu, *Inorg. Chem.*, 2012, **51**, 3972–3980.
65 N. L. Fry and P. K. Mascharak, *Dalton Trans.*, 2012, **41**, 4726–4735.
66 N. L. Fry, X. P. Zhao and P. K. Mascharak, *Inorg. Chim. Acta*, 2011, **367**, 194–198.
67 A. C. Merkle, N. L. Fry, P. K. Mascharak and N. Lehnert, *Inorg. Chem.*, 2011, **50**, 12192–12203.
68 G. Frenking, I. Fernández, N. Holzmann, S. Pan, I. Krossing and M. Zhou, *JACS Au*, 2021, **1**, 623–645.
69 A. J. Lupinetti, S. Fau, G. Frenking and S. H. Strauss, *J. Phys. Chem. A*, 1997, **101**, 9551–9559.
70 A. S. Goldman and K. Krogh-Jespersen, *J. Am. Chem. Soc.*, 1996, **118**, 12159–12166.
71 D. M. P. Mingos, in *Nitrosyl Complexes in Inorganic Chemistry, Biochemistry and Medicine I*, ed. D. M. P. Mingos, Springer, Berlin, Heidelberg, 2014, pp. 1–44, DOI: **10.1007/430_2013_116**.
72 H. Lewandowska, in *Nitrosyl Complexes in Inorganic Chemistry, Biochemistry and Medicine I*, ed. D. M. P. Mingos, Springer, Berlin, Heidelberg, 2014, pp. 117–124, DOI: **10.1007/430_2013_109**.
73 M. Madhani, A. K. Patra, T. W. Miller, A. A. Eroy-Reveles, A. J. Hobbs, J. M. Fukuto and P. K. Mascharak, *J. Med. Chem.*, 2006, **49**, 7325–7330.
74 P. K. Mascharak, *J. Inorg. Biochem.*, 2022, **231**, 111804.
75 A. A. Eroy-Reveles, Y. Leung and P. K. Mascharak, *J. Am. Chem. Soc.*, 2006, **128**, 7166–7167.
76 G. M. Halpenny, K. R. Gandhi and P. K. Mascharak, *ACS Med. Chem. Lett.*, 2010, **1**, 180–183.
77 B. J. Heilman, G. M. Halpenny and P. K. Mascharak, *J. Biomed. Mater. Res., Part B*, 2011, **99**, 328–337.
78 B. J. Heilman, J. St. John, S. R. J. Oliver and P. K. Mascharak, *J. Am. Chem. Soc.*, 2012, **134**, 11573–11582.